Plasma-assisted molecular beam epitaxy of SnO(001) films: Metastability, hole transport properties, Seebeck coefficient, and effective hole mass

Melanie Budde,[1] Piero Mazzolini,[1] Johannes Feldl,[1] Christian Golz,[2] Takahiro Nagata,[3] Shigenori Ueda,[3,4] Georg Hoffmann,[1] Manfred Ramsteiner,[1] and Oliver Bierwagen,[1]

[1)] *Paul-Drude-Institut für Festkörperelektronik, Leibniz-Institut im Forschungsverbund Berlin e.V., Hausvogteiplatz 5-7, 10117 Berlin, Germany*

[2)] *Department of Physics, Humboldt-Universität zu Berlin, Newtonstrasse 15, 12439 Berlin, Germany*

[3)] *National Institute for Materials Science (NIMS), Tsukuba, Ibaraki 305-0044, Japan*

[4)] *Synchrotron X-ray Station at SPring-8, NIMS, Sayo, Hyogo 679-5148, Japan*

(Dated: August 4, 2020)

arXiv:2007.13448v2 [cond-mat.mtrl-sci] 3 Aug 2020

Transparent conducting or semiconducting oxides are an important class of materials for (transparent) optoelectronic applications and – by virtue of their wide band gaps – for power electronics. While most of these oxides can be doped n-type only with room-temperature electron mobilities on the order of $100\,\mathrm{cm^2/Vs}$, p-type oxides are needed for the realization of pn-junction devices but typically suffer from exessively low ($<<1\,\mathrm{cm^2/Vs}$) hole mobilities. Tin monoxide (SnO) is one of the few p-type oxides with a higher hole mobility yet is currently lacking a well-established understanding of its hole transport properties. Moreover, growth of SnO is complicated by its metastability with respect to SnO_2 and Sn, requiring epitaxy for the realization of single crystalline material typically required for high-end applications. Here, we give a comprehensive account on the epitaxial growth of SnO, its (meta)stability, and its thermoelectric transport properties in the context of the present literature. Textured and single-crystalline, unintentionally-doped p-type SnO(001) films are grown on Al_2O_3(00.1) and Y_2O_3-stabilized ZrO_2(001), respectively, by plasma-assisted molecular beam epitaxy and the epitaxial relations are determined. The metastability of this semiconducting oxide is addressed theoretically through an equilibrium phase diagram. Experimentally, the related SnO growth window is rapidly determined by an in-situ growth kinetics study as function of Sn-to-O-plasma flux ratio and growth temperature. The presence of secondary Sn and SnO_x ($1 < x \leq 2$) phases is comprehensively studied by x-ray diffraction, Raman spectroscopy, scanning electron microscopy, and x-ray photoelectron spectroscopy, indicating the presence of Sn_3O_4 or Sn as major secondary phases, as well as a fully oxidized SnO_2 film surface. The hole transport properties, Seebeck coefficient, and density-of-states effective mass are determined and critically discussed in the context of the present literature on SnO, considering its strongly anisotropic effective hole mass: Hall measurements of our films reveal room temperature hole concentrations and mobilities in the range of $2\cdot10^{18}$ to $10^{19}\,\mathrm{cm^{-3}}$ and 1.0 to $6.0\,\mathrm{cm^2/Vs}$, respectively, with consistently higher mobility in the single-crystalline films. Temperature-dependent Hall measurements of the single-crystalline films closest to stoichiometric, phase-pure SnO indicate non-degenerate band transport by free holes (rather than hopping transport) with dominant polar optical phonon scattering at room temperature. Taking into account the impact of acceptor band formation and the apparent activation of the hole concentration by 40–53 meV, we assign tin vacancies rather than their complexes with hydrogen as the unintentional acceptor. The room temperature Seebeck coefficient in our films confirms p-type conductivity by band transport. Its combination with the hole concentration allows us to experimentally estimate the density of states effective hole mass to be in the range of 1 to 8 times the free electron mass.

I. INTRODUCTION

Most of the used semiconducting oxides are n-type, reducing the applications of semiconducting oxides mainly to unipolar devices. This is in part related to the low hole mobilities arising from the strong localization of the O $2p$ orbitals that make-up the valence band maxima (VBM) with little dispersion, i.e. high hole effective mass. For example, the hole mobility in the p-type semiconducting oxides NiO:Li,[1] NiO,[2] Cr_2O_3:Mg,[3] and $LaScO_3$:Sr[4] is significantly lower than $1\,\mathrm{cm^2/Vs}$, being best described by polaronic hopping instead of band transport.[2,5] As a solution hybridization between O $2p$ and more spread orbitals by the concept known as "chemical modulation of the valence band" has been proposed to increase the dispersion of the VBM and thus decrease the hole effective mass.[6]One candidate for hybridization are lone-pair ns^2 orbitals.[5] For example, $5s^2$ in Sn^{2+} of SnO forms a stable configuration with the O $2p$ orbitals, making SnO an interesting material for p-type oxide electronics.[5] In fact, hole mobilities between 1 and 5 $\frac{\mathrm{cm^2}}{\mathrm{Vs}}$ have typically been obtained by Hall measurements of SnO films.[5,7–10] More recently, hole mobilities as high as 30, 21, and 19 $\frac{\mathrm{cm^2}}{\mathrm{Vs}}$ have been reported for polycrystalline SnO bulk ceramics,[11] optimized epitaxial SnO(001) layers,[12] and polycrystalline, mixed SnO+Sn films,[13] respectively. Thus, reasonably high hole mobilities together with a direct bandgap absorption edge

around 2.6–3.2 eV (and only weak optical absorption by its indirect band gap of 0.6 eV),[5,7,8] fuel the interest in SnO as a p-type semiconducting oxide for transparent thin film transistor applications.[10] The observed p-type conductivity of unintentionally doped (UID) SnO has been correlated by first-principle calculations with Sn vacancies[14] or their complexes with hydrogen[15] acting as shallow acceptors, whereas oxygen interstitials were predicted to be electrically inactive.[14,15]

SnO thin films have been grown by various methods, such as electron-beam evaporation[16] or reactive DC magnetron sputtering,[13] both followed by thermal annealing, reactive ion beam sputter deposition,[9] pulsed laser deposition (PLD) from an oxide target[10,12,17] or a metallic Sn target[18], and molecular beam epitaxy (MBE).[8,19,20] The largest challenge for the growth of phase pure SnO is its metastability with respect to its stable relatives Sn and SnO_2.

At present the MBE growth of SnO is a rather unexplored field with reports on the formation of polycrystalline SnO from the Sn-vapor in the presence of pyrolyzed NO_2[19] or reactive oxygen (followed by an annealing step)[20]. Using MBE phase-pure, single crystalline SnO(001) films have so far only been realized by subliming SnO_2 source material onto the heated r-plane sapphire substrate without supplying additional oxygen.[8] This is related to the fact that sublimation of SnO_2 produces gaseous SnO and oxygen species.[21]

In this study, we demonstrate the growth of textured and single-crystalline SnO(001) films on Al_2O_3(00.1) and Y_2O_3-stabilized ZrO_2(001) [YSZ(001)], respectively, from the Sn-vapor using oxygen plasma-assisted MBE. After discussing the temperature-composition phase diagram of the Sn-O-system obtained from thermochemical considerations, we experimentally establish the related growth window using in-situ analytics of the growth rate of SnO_2 and the desorption of SnO from the growth front. The formed phase(s), epitaxial relation to the substrate, and structural properties of films grown at different conditions are shown. The hole transport properties are determined and discussed in the context of existing literature on SnO. In particular, the room-temperature hole concentration and Seebeck coefficient of all films are determined and utilized to estimate the density-of-states effective hole mass. Temperature-dependent hole transport properties reveal band transport with a hole mobility limited by polar optical phonon scattering and a free-hole activation energy of 53 meV which is compared to theoretically predicted acceptor ionization energies.

II. EXPERIMENT

SnO_x films were grown by plasma assisted molecular beam epitaxy as generally described in Ref. 22 on 2-inch c-plane sapphire [Al_2O_3(00.1)] or quarters of 2-inch YSZ(001) substrates. Both types of substrates were covered with 1 µm titanium by sputter deposition on the rough backside to improve its radiative heating from the SiC heating filament. The growth temperature T_g was measured by a thermocouple between substrate and heating filament. To improve heating and layer uniformity the substrate was continuously rotated at two rotations per minute. Sn (7N purity) was evaporated from a shuttered single filament effusion cell operated at 1175 °C, resulting in a beam equivalent pressure of $\approx 1.2 \cdot 10^{-7}$ mbar at the substrate position. Activated oxygen was provided by passing a controlled flow of O_2 (6N purity) through a radio-frequency (RF) plasma source (run at a fixed RF power of 300 W) directed at the substrate. Before growth a 20–30 min oxygen plasma cleaning was performed at T_g =700 °C and an oxygen flux of 0.5 standard cubic centimeters per minute (sccm). After that the substrate temperature was ramped to the desired growth temperature and the oxygen flux was reduced to the desired growth flux (f_g). Growth was initiated and terminated by opening and closing the Sn-shutter, respectively. After film growth the substrate temperature was ramped down at 0.5°C/s to 200 °C under the O-plasma (using the O-flux as during growth) followed by further cooldown to room temperature in vacuum.

The growth rate and amount of desorbing ^{136}SnO was measured in-situ using laser reflectometry (LR) and line-of-sight quadrupole mass spectrometry (QMS), respectively, as described in Ref. 22. These measurements allowed us to determine the growth window of SnO on c-plane sapphire substrates. Afterwards, individual SnO_x layers were grown on Al_2O_3(0001) and YSZ(001) at slightly different growth conditions.

These SnO_x layers were structurally investigated by X-ray diffraction (XRD) and Raman spectroscopy. XRD was measured in a four-circle diffractometer using Cu Kα-radiation and a 1 mm detector slit. The Raman spectroscopic measurements were performed at room temperature in the backscattering geometry with optical excitation at wavelengths of 473 nm (photon energy of 2.61 eV) by a solid-state laser and at 325 nm (3.81 eV) by a He-Cd laser. The incident laser light was focused by a microscope objective onto the sample surface. The backscattered light was collected by the same objective, spectrally dispersed by an 80-cm spectrograph and detected by a liquid-nitrogen-cooled charge-coupled device. The Raman spectra were recorded in the polarized configuration (parallel polarizations of incoming and scattered light) using a linear polarizer to analyze the detected light. Top-view scanning electron microscopy (SEM) images were taken from all films.

On a selected sample, qualitative depth profiling of the valence band structure and Sn $3d_{5/2}$ core level was performed by photoelectron spectroscopy taking advantage of the dependence of the photoelectron mean free path $\lambda = \lambda_0 \times \cos(\mathrm{TOA})$ on the take-off-angle (TOA, 0° corresponds to normal emission) and kinetic energy of the photoelectron (equalling the difference of photon energy and binding energy) using soft X-rays (1468.6eV,

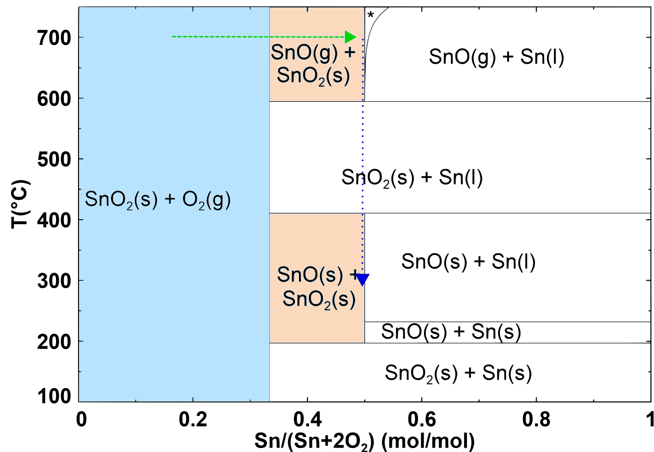

Figure 1. Equilibrium phase diagram of the Sn-O system as function of stoichiometry and temperature at a typical pressure in the MBE growth chamber of 10^{-6} mbar. Stoichiometries of $n_{\text{Sn}}/(n_{\text{Sn}}+2n_{O_2})$ = 0, 1/3, 1/2, and 1 correspond to pure O_2, SnO_2, SnO, and Sn, respectively. Constituents labeled "(s)", "(l)" and "(g)", are solid, liquid, and gaseous, respectively. The phase labeled "*" denotes SnO(g) + Sn(g). For comparison to Fig. 2 the light blue and light orange shaded areas corresponds to an oxygen-rich and tin-rich growth regime of SnO_2, respectively, and the green and blue arrows indicate the used strategy of determining the growth window for SnO-growth as described in the following sub-section.

$\lambda_0 \approx 1.8$ nm in SnO, Thermo Sigma-probe XPS system, SXPES) for surface sensitivity as well as hard X-rays (HAXPES, 5956.3 eV, $\lambda_0 \approx 6.9$ nm in SnO, beamline BL15XU at the Spring-8 synchrotron[23]) for bulk sensitivity as described in Ref. 24. Measurements were performed using the TOAs of 9.7, 54.7, 84.7 and 5.0, 50.0, 70.0° in SXPES and HAXPES, respectively.

In addition, Seebeck and Hall measurements in the van-der-Pauw geometry, as described in Ref. 25, were used to investigate the transport properties of the different layers at room temperature. Temperature dependent Hall measurements on a selected SnO sample were performed as described in Ref. 26.

The thermal stability of the SnO phase was investigated using rapid thermal annealing (RTA) at diffrent tempratures in nitrogen, oxygen and forming gas ($N_2 + H_2$) at atmospheric pressure. In addition, the stability under storage in air was investigated by regular Hall measurements of a film over a period of 120 days.

III. THERMODYNAMICS OF THE GROWTH WINDOW

Common challenges for the growth of phase-pure SnO are its metastability with respect to the disproportionation into SnO_2 and Sn, as well as the adjustment of the stoichiometry to prevent the formation of secondary SnO_2 or Sn phases. Fig. 1 illustrates this situation with the help of the equilibrium Sn-O phase diagram calculated by the FactSage 7.3 software package[27] as a function of stoichiometry $n_{\text{Sn}}/(n_{\text{Sn}}+2n_{O_2})$ and temperature. While solid phases [labeled by "(s)"] of Sn, SnO, and SnO_2 are present, the calcuations did not predict stability of the intermediate oxides Sn_2O_3 and Sn_3O_4. Note that despite the non-equilibrium nature of thin film growth, equilibrium phase diagrams can provide guidance as discussed next: Firstly, the stability region of SnO at temperatures between 197 and 410 °C (and disproportionation outside this region) rationalizes why most SnO films have been obtained at growth or annealing temperatures in this temperature range;[7–9,12,17,20] secondly, during growth by reactive sputtering[9,13], PLD,[10,18] or MBE[19] the formation of secondary SnO_2 or Sn-phases has been controlled by adjusting the stoichiometry of the source vapor, i.e., the oxygen (background) pressure at fixed flux of SnO_x from the source, in qualitative agreement with the equilibrium stoichiometry dependence in the phase diagram. The blue or orange shaded regions as well as colored arrows in Fig. 1 indicate the relation to the in-situ determination of the growth window discussed next.

IV. RAPID IN-SITU KINETIC DETERMINATION OF THE GROWTH WINDOW

We have previously demonstrated that suboxide-possessing binary oxides generally grow in MBE by a two-step kinetics through intermediate suboxide formation.[28] For example, during the growth of SnO_2, Sn is oxidized to the suboxide SnO (Sn + O → SnO) in the first step. In the second step SnO is further oxidized to SnO_2 (SnO + O → SnO_2) if sufficient oxygen is available. Thus, at a sufficiently high Sn/O flux ratio the second step is suppressed, preventing the growth of SnO_2. In addition, a sufficiently high growth temperature leads to desorption of the intermediate SnO that does not get further oxidized and thus does not contribute to film growth.[29]

By taking advantage of this behavior we determined the stoichiometric metal to oxygen flux ratio for the SnO formation by simultaneously measuring the growth rate of SnO_2 and the desorption of SnO in-situ on a single Al_2O_3(0001) substrate at T_g = 700 °C, which is high enough to result in desorption of SnO that cannot get further oxidized. In contrast to Refs. 22,29, in which the growth rates for varying Sn flux are discussed at fixed O-flux, we kept the Sn-flux constant and gradually decreased the O-flux from f_g = 1.0 to 0.2 sccm, which corresponds to a transition from the SnO_2(s) + O_2(g) to the SnO(g) + SnO_2(s) phase (green, dashed arrow in Fig. 1). The corresponding diagram shown in Fig 2 exhibits a constant, high SnO_2 growth rate without SnO desorption for f_g ranging from 1 sccm to 0.36 sccm (blue shaded region). This bevavior indicates oxygen-rich growth conditions under which the entire Sn-flux is oxidized to SnO_2,[22,28,29] corresponding to a stoichiometry in the region of the

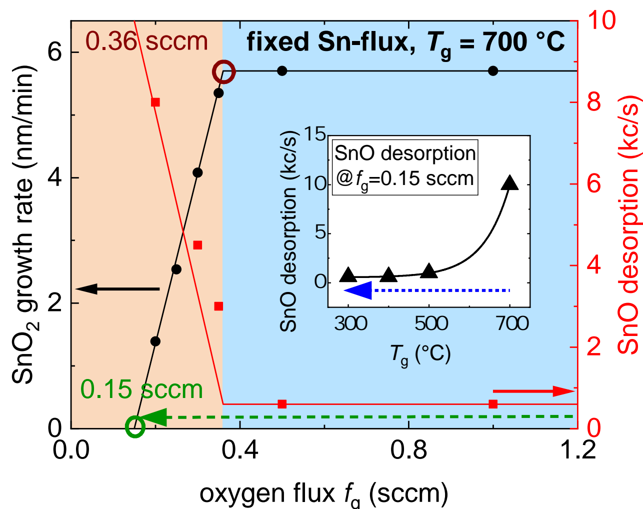

Figure 2. SnO_2 growth rate (black discs) and desorbing SnO flux (red squares) as function of oxygen flux, identifying two growth regimes: oxygen rich (blue) and metal rich (orange). Red and black lines are guides to the eye. The inset shows the desorbing SnO flux at fixed oxygen flux as a function of growth temperature. To facilitate comparison to the phase diagram the green dashed and blue dotted arrows correspond to those in Fig. 1.

$SnO_2(s) + O_2(g)$ phase in Fig. 1. Decreasing f_g from 0.36 sccm (orange shaded region) leads to a decreasing SnO_2 growth rate and simultaneously increasing SnO desorption, indicative of Sn-rich growth conditions[22,28,29] and a corresponding stoichiometry in the region of the $SnO(g) + SnO_2(s)$ phase in Fig. 1. In this case part of the SnO which is formed in the first step desorbs due to an insufficient O-flux for the second oxidation step.[28] Consequently, the extrapolated $f_g = 0.15$ sccm at which SnO_2 growth ceases corresponds to the complete suppression of the second oxidation step, an Sn/O-flux ratio for stoichiometric SnO formation, and the phase boundary between $SnO(g) + SnO_2(s)$ and $SnO(g) + Sn(l)$ at $n_{Sn}/(n_{Sn} + 2n_{O_2}) = 0.5$ (marked by the end of the green arrow) in Fig. 1.

Next, we determined the T_g-dimension of the SnO growth window at the approximately stoichiometric oxygen flux of 0.15 sccm for SnO formation by measuring the desorbing SnO-flux in-situ in the range of 300 °C≤ T_g ≤700°C on the same Al_2O_3(00.1) substrate, corresponding to the blue, dotted arrow in Fig. 1. The results shown in the inset of Fig. 2 reveal negligible SnO desorption at $T_G \leq 500$ °C, indicating the growth of solid SnO at the used fluxes.

V. EPITAXIAL GROWTH, PHASES, EPITAXIAL RELATION

Individual SnO_x thin film samples were epitaxially grown on YSZ(001) and Al_2O_3(00.1) within the delineated growth window and the formed phases and structural properties were determined. The following crystal structures and phases can (potentially) be found in the grown samples: YSZ crystallizes in the cubic, fluorite structure with a lattice parameter of about $a = 0.512$ nm, whereas sapphire (Al_2O_3) possesses the corundum structure with lattice parameters $a = 0.4763$ nm and $c = 1.3003$ nm. Sn crystallizes in a tetragonal structure with lattice parameters $a = 0.583$ nm and $c = 0.318$ nm.[30] The best documented and most stable SnO_x phases are the tetragonal rutile SnO_2 with lattice parameters of $a = 0.474$ nm and $c = 0.319$ nm,[31] and tetragonal α-SnO with $a = 0.380$ nm, $c = 0.484$ nm.[32] In addition, the intermediate phases Sn_2O_3 and Sn_3O_4 have been identified in the past both with monoclinic as well as triclinic crystal structures. The monoclinic structure has been theoretically predicted for both stoichiometries by the cluster expansion technique[33] and by ab initio calculations.[34] In an early experimental paper Lawson identified the triclinic structure for Sn_3O_4 using XRD,[35] whereas later White et al. determined Sn_3O_4 to be monoclinic by precession electron diffraction measurements.[36] For Sn_2O_3 a triclinic phase has been identified using powder diffraction by Murken and Trömel[37] and has been confirmed by Kuang et al.[38] for nanostructures formed by a hydrothermal method. The 2Θ- angles of XRD reflexes of the triclinic phases of Sn_2O_3[37] and Sn_3O_4[35] are similar enough to impede an unambiguous distinction of both phases by XRD. Likewise, the spread of theoretically and experimentally determined crystal structures and lattice parameters for Sn_3O_4 and related 2Θ- angles of XRD reflexes make it difficult to unambiguously distinguish Sn_3O_4 from other SnO_x phases (including Sn) by XRD.

Raman spectroscopy is a powerful alternative method for phase identification. In contrast to XRD, Raman spectra of monoclinic and triclinic Sn_3O_4 do not differ drastically.[34,39] Furthermore, Eifert et al. have predicted distinctly different Raman spectra for monoclinic Sn_3O_4 and Sn_2O_3 by first principles calculations.[34] In a series of SnO_x samples prepared by ion-beam sputtering with x varying from 1 to 2, they have only identified the presence of Sn_3O_4 as intermediate phase by Raman spectroscopy.[34] In agreement with that work we have not identified spectral features which could be assigned to Sn_2O_3 in Raman spectra of our films, either, and will therefore focus on Sn_3O_4 as intermediate phase. The measured Raman spectra of all our epitaxial films are, in general, well described by a superposition of contributions from different oxide phases in addition to spectral features originating from the substrate and metallic Sn in certain cases. The peak positions of the dominant Raman peaks expected for the oxide phases SnO,[34,40,41] SnO_2,[34,42,43], and Sn_3O_4[34,39,41,44] as well as metallic Sn[45] are indicated in Figs. 3(c,d) and 4(c,d) as vertical dashed lines. In the case of SnO_2 it has been taken into account that for the polarization configuration of our experiments only the A_{1g} phonon mode at 638 cm^{-1} can be observed.[42]

Whereas the optical probing depth $(\alpha_i+\alpha_s)^{-1}$ in SnO is 260 nm for excitation at 2.62 eV, only 5 nm below the surface is probed when excitation at 3.81 eV is chosen (α_i and α_s are the absorption coefficents at the photon energies of the incoming and scattered light, respectively, taken from Ref. 8). Consequently, the bulk properties of epitaxial films consisting mainly of SnO can be investigated when using excitation at 2.62 eV (similar to the case of XRD measurements), while at 3.81 eV just the near surface layers are probed. Regarding the sensitivity for different oxide phases, it has to be considered that the dielectric function $\epsilon(\omega)$ of SnO[8] and the absorption spectrum of Sn_3O_4[44] exhibit maxima in the near ultraviolet spectral range which are connected with large absolute values of the derivative $|d\epsilon/d\omega|$ both at photon energies of 2.6 and 3.8 eV. Under this prerequisite, strong resonance enhancements in efficiency of Raman scattering are expected.[46,47] For SnO_2, in contrast, the onset of strong optical absorption at 4.28 eV extracted from the ordinary diecelectric function does not result in a particularly large value of $|d\epsilon/d\omega|$.[48] As a consequence, the sensitivity for the detection of Raman signals is expected to be better for SnO and Sn_3O_4 compared to SnO_2 at both excitation energies (2.62 and 3.81 eV) chosen for our experiments.

A. Growth on Al_2O_3(00.1) at different temperatures

Three samples, A500, A400, and A300, were grown for ≈ 30 min on individual Al_2O_3(00.1) substrates at fixed f_G = 0.15 sccm and T_g =500 °C, 400 °C, and 300 °C, respectively. Fig. 3 shows structural informaton of the resulting films obtained by XRD, SEM, and Raman scattering.

For sample A500, XRD [Fig. 3(a)] indicates only the presence of trigonal Sn_3O_4,[35] and possibly SnO_2 and Sn (whose 2Θ angles overlap with those from Sn_3O_4). In agreement, bulk sensitive Raman scattering [Fig. 3(c)] indicates a strong contribution from Sn_3O_4 but also weak SnO-related peaks. Surface sensitive Raman scattering [Fig. 3(d)] shows additional minor fractions of Sn. The absence of a major fraction of SnO shown by all these results is in qualitative agreement with a disproportionation of SnO at temperatures above 410°C predicted by the phase diagram (Fig. 1). Different from the phase diagram, however, Sn_3O_4 instead of SnO_2 is formed as major oxide phase. The SEM image shows a ≈ 300 nm-thick, porous, polycrystalline layer.

Better ordered, ≈ 130 nm-thick films (A400 and A300) were obtained at growth temperatures of 400 and 300°C as shown by the corresponding SEM images [Fig. 3(b)]. XRD of these films [Fig. 3(a)] shows only the SnO(002) reflex besides the (00.6) one of the Al_2O_3 substrate, indicating phase-pure SnO, in agreement with the stability region for SnO at these temperatures in the phase diagram (cf. Fig. 1). The phase purity is corroborated by the bulk sensitive Raman spectra [Fig. 3(c)]. A slightly higher crystal quality at 400 °C is signified by the sharper SnO(002) peak and the lower full width at half maximum (FWHM) of the ω-rocking curve of the SnO(002) reflex (1.1° and 1.9° for A400 and A300, respectively, not shown). The mismatch of rotational symmetry [6-fold for the Al_2O_3(00.1) surface and 4-fold for the SnO(001) film] is predicted to result in three rotational domains,[49] which is indeed reflected by the 12 SnO{101} peaks in the skew symmetric Φ-scan of A400 shown in the inset of Fig. 3(a). The three Al_2O_3{10.2}-peaks in the Φ-scan (indicating the three-fold bulk rotational symmetry of the corundum structure) appear at values of Φ that coincide with {101} peaks of the SnO film on top of the substrate. From these data we can establish the out-of-plane and in-plane epitaxial relation of SnO on c-plane Al_2O_3 as:

$$\mathrm{SnO}(001)\,||\,\mathrm{Al_2O_3}(00.1)\text{ for all domains, and}$$

$$\mathrm{SnO}(100)\,||\,\mathrm{Al_2O_3}(01.0),(-11.0),\text{and }(0-1.0)\\ \text{for domains 1–3, respectively.}$$

Interestingly, the surface sensitive Raman spectra [Fig. 3(d)] show Sn_3O_4 peaks with similar strengths as the SnO-related ones in A400 and A300, indicating an oxidized surface, likely related to the cooldown of the film to 200°C in oxygen plasma after growth. The stronger Sn_3O_4 peak intensity of A400 compared to that of A300 would also agree with the longer time under oxygen plasma during cooldown for A400 allowing a deeper oxidation of the SnO surface. [Please note that the relative intensities of the B_{1g} (115 cm^{-1}) and A_{1g} (210 cm^{-1}) phonon lines from SnO are obviously influenced by individual resonance enhancements occuring for excitation at 2.62 and 3.81 eV, respectively.] The platelets seen in the SEM image of A400 [Fig. 3(b)] show a striking similarity to those of hydrothermally synthesized Sn_3O_4[50], further corroborating the assignment of this surface phase.

B. Growth on YSZ(001) at different O-fluxes

Based on the highest crystalline quality of the SnO in A400 a growth temperature of 400 °C was chosen for the subsequent growth experiments using YSZ(001) substrates. The four-fold rotational symmetry of this cubic substrate matches that of the SnO(001) surface and has been shown to prevent the formation of rotational domains in PLD-grown films.[10,17] Four different oxygen fluxes (0.18 sccm, 0.15 sccm, 0.12 sccm and 0.10 sccm) in the vicinity of the stoichiometric flux of 0.15 sccm (extrapolated in Fig. 2) were used to study their impact on phase formation. Fig. 4 shows the structural data of the resulting four, ≈ 120 nm-thick films (Y18, Y15, Y12, and Y10, respectively). The sample Y18 (0.18 sccm) shows only weak XRD peaks [Fig. 4(a)] likely related to the polycrystalline, disordered struc-

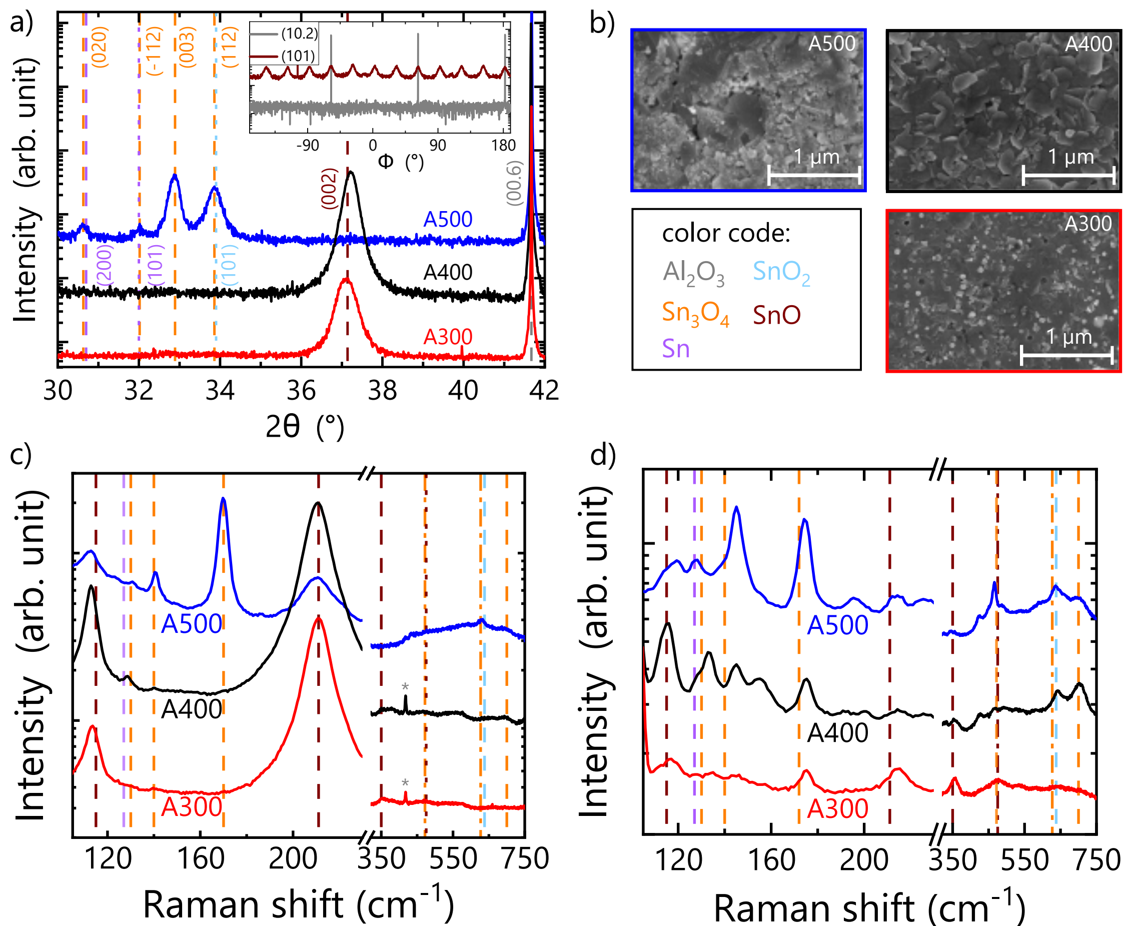

Figure 3. Structural characterization of SnO films grown on $Al_2O_3(00.1)$ at different substrate temperature. a) XRD symmetric out-of-plane $2\Theta-\omega$ scan. Vertical lines indicate the expected positions of reflexes of different phases as indicated by color code on the right hand side. The inset shows a Φ-scan of skew symmetric substrate and SnO reflexes as indicated of A400. (b) Top view SEM images. (c) Bulk-sensitive and (d) surface-sensitive Raman spectra measured with an excitation wavelength of 473 and 325 nm, respectively. Vertical lines indicate the peak positions of dominant Raman active phonon modes expected for different phases as indicated by the color code in (b). The Raman peak marked by "*" is substrate related.

ture visible in the SEM image [Fig. 4(b)]. The related Raman spectrum [Fig. 4(c)] shows Sn_3O_4-related peaks and a weak SnO contribution, in agreement with the O-rich flux stoichiometry. In contrast, the layers grown at lower oxygen flux (0.15 − 0.10 sccm, Y15 − Y10) are showing strong SnO(002) XRD peaks [Fig. 4(a)] as well as dominant SnO-related bulk sensitive Raman peaks [Fig. 4(c)], indicative of a dominant SnO phase, forming a smooth, compact layer as seen in the SEM images [Fig. 4(c)]. At an oxygen flux of 0.15 sccm, however, a broad XRD peak around $2\Theta = 33°$ exists that could be assigned to a secondary Sn_3O_4 phase according to the weak additional bulk-sensitive Raman peaks and likely visible as crystallites protruding from the film surface. The films grown at 0.12 and 0.10 sccm, in contrast, are phase pure gauged by XRD and bulk-sensitive Raman spectra but exhibit droplets visible in the SEM images, suggesting metallic Sn as a secondary phase. In the context of the phase diagram Fig. 1 an O-flux of 0.15 sccm corresponds to an O-rich stoichiometry with associated phase "$SnO(s) + SnO_2(s)$", whereas 0.12 sccm correspond to a Sn-rich stoichiometry with associated phase "$SnO(s) + Sn(l)$". Also the films grown on YSZ show that, different from the phase-diagram, under slightly O-rich conditions the intermediate Sn_3O_4 rather than SnO_2 is formed as major secondary oxide phase.

The SnO(002) XRD reflex of Y15, Y12, and Y10 shows a ω-rocking curve FWHM of 0.67°, 0.46°, and 0.51°, respectively. The insets of [Fig. 4(a)] show the Φ-scan of Y12 and the related in-plane epitaxial relation between SnO(001) and YSZ(001) characterized by a 45° rotation with respect to each other, which reduces the mismatch from -34 % ($a_{SnO} = 0.38$ nm, $a_{YSZ} = 0.51$ nm) to 5 % ($2a_{SnO} = 0.76$ nm, $\sqrt{2}a_{YSZ} = 0.72$ nm). These data agree with the out-of-plane and in-plane epitaxial relation SnO(001) || YSZ(001) and SnO(110) || YSZ(100), respectively, reported in Refs. 10,17 for PLD-grown films.

The surface sensitive Raman spectra shown in

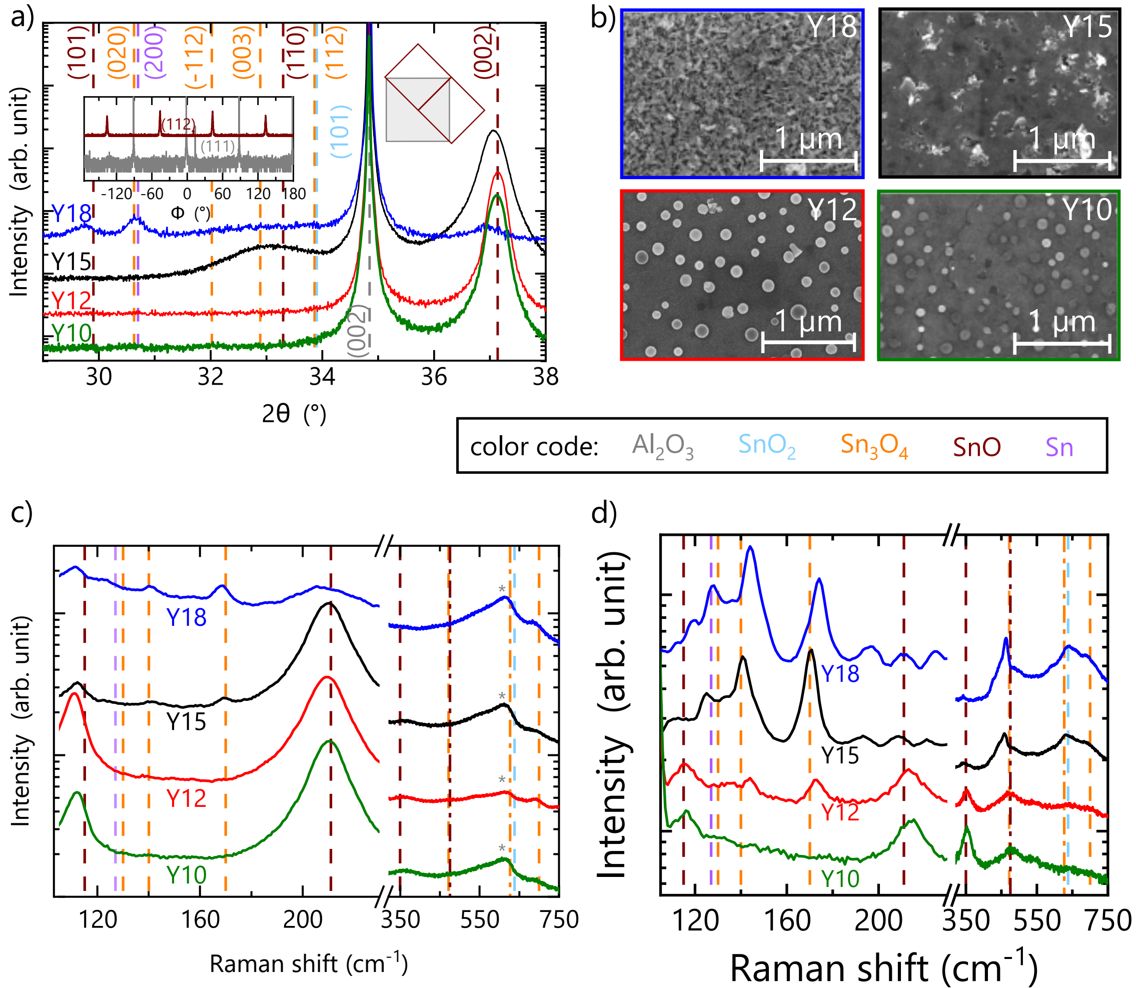

Figure 4. Structural characterization of SnO films grown on YSZ(001) as function of oxygen flux f_G. (a) XRD symmetric out-of-plane $2\Theta - \omega$ scan. Vertical lines indicate the expected positions of reflexes of different phases as indicated by color code on the right hand side. The insets show a Φ-scan of skew symmetric substrate and SnO reflexes as indicated of the sample grown at 0.12 sccm, as well as a pictorial representation of the 45° rotated SnO unit cell for better lattice match. (b) Top view SEM images. (c) and (d) Bulk -and surface-sensitive Raman spectra measured with an excitation wavelength of 473 and 325 nm, respectively. Vertical lines indicate the position of strong Raman active peaks due to different phases as indicated by color code on the right hand side. The Raman peak marked by "*" is substrate related.

[Fig. 4(d)] indicate pure Sn_3O_4 for samples Y18 and Y15, dominant SnO with a weak Sn_3O_4 contribution for Y12, and pure SnO for Y10.

Bulk- and surface sensitive Photoelectron Spectroscopy

Sample Y10 was further analyzed by photoelectron spectroscopy. The Sn $3d_{5/2}$ core level, exemplarily shown in Fig. 5(a), consists of up to three contributions that are related to an increasing oxidation state at increasing binding energy. The lowest binding energy contribution (at ≈ 485 eV) can be attributed to metallic Sn (Sn^0), that at ≈ 486 eV to SnO (Sn^{2+}), and that at ≈ 487 eV to SnO_2 (Sn^{4+}).[52–54] The intensity of the contributions of the different oxidation states normalized to the total peak intensity is shown in Fig. 5(b) as a function of photoelectron mean free path λ ($\lambda < 2$ nm mesaured by SXPES and $\lambda > 2$ nm by HAXPES). The inset shows the depth-dependent detection probability for photoelectrons for two different λ that correspond to normal emission HAXPES (6.9 nm) and SXPES (1.8 nm). Even though the detection probability is highest for photoelectrons from the surface in both cases, HAXPES provides a larger fraction of photoelectrons from deeper regions than SXPES. Consequently, Fig. 5(b) can be discussed as a qualitative depths profiling of the different Sn-related phases present in the near-surface region of the film: The dominant contribution is stemming from Sn^{4+} and makes up ≈ 90 % of the peak intensity within the first 2 nm, which can only be explained by a SnO_2 surface layer. The valence band spectrum taken by surface-sensitive SXPES

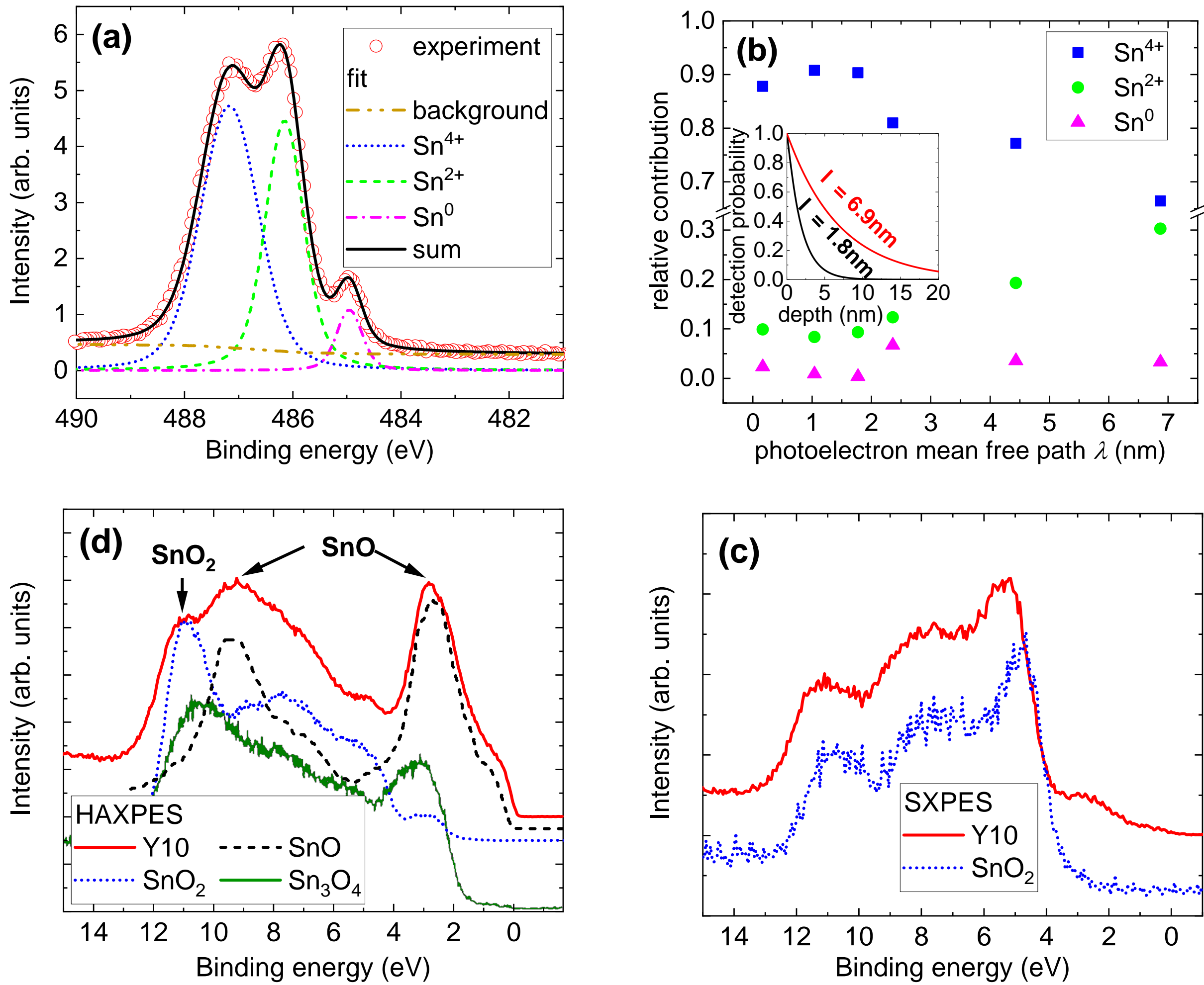

Figure 5. Photoelectron spectra of sample Y10. The binding energy scale is calibrated such that 0 eV correspond to the Fermi level. (a) Representative Sn $3d_{5/2}$ core level measured by bulk-sensitive HAXPES and its decomposition into contributions of different Sn valence states as labeled. (b) Relative contribution of the different Sn-valence states to the total Sn $3d_{5/2}$ core level as function of detection depth (photoelectron mean free path λ) measured by SXPES (0–2 nm) and HAXPES (2–7 nm) at different TOA. The inset shows probability distributions of photoelectron detection as function of depth for SXPES ($\lambda = 1.8$ nm) and HAXPES ($\lambda = 6.9$ nm) for the lowest TOAs used in this study (9.7 and 5° for SXPES and HAXPES, respectively).(c) and (d) Valence band spectrum of Y10 (red, solid line) along with that of a bulk SnO_2 reference sample (blue dashed line, taken from Ref. 24), SnO(001) thin film grown by PLD taken and adapted from Ref. 51, as well as Sn_3O_4 taken and adapted from the supporting information of Ref. 50. Measurements accomplished with HAXPES at TOA=5° are bulk sensitive (c) while those measured by SXPES at TOA=9.7° are surface sensitive (d).

resembles that of a pure SnO_2 bulk sample (taken from Ref. [24]) as shown in Fig. 5(d). It thus corroborates the assignment of a few-nm thick SnO_2 surface layer, similar to findings on air-exposed SnO MBE-grown from the SnO vapor.[8] With increasing λ the Sn^{4+} contribution decreases whereas the Sn^{2+} contribution steadily increases from 10 % at the surface reaching 30 % at the maximum probed depth ($\lambda = 6.9$ nm). This could in principle be related to the presence of the mixed-valence tin oxide Sn_3O_4 $[(Sn^{2+})_2(Sn^{4+})O_4]$[50] below the surface. In agreement with the absence of Sn_3O_4 in the surface-sensitive Raman spectrum of Y10 [Fig. 4(d)] the valence band spectrum of Y10 shown in Fig. 5(c) taken by bulk-sensitive HAXPES, however, does not match that of the Sn_3O_4 (shown in the supporting information of Ref. 50). Instead, the valence band spectrum resembles that of SnO(001) with a small contribution of SnO_2 from the surface photoelectrons as comparison to the reference HAXPES spectra of SnO_2[24] and SnO(001)[51] [also shown in Fig. 5(c)] yields. Both contributions are labeled. The shoulder at 1 eV, which is also present in HAXPES from the PLD-grown SnO(001)[51] may indicate the presence of metallic Sn,[52] leading to a valence spectrum similar to that shown for Sn-added *p*-type SnO films in Ref. 55. This assignment would agree with a small but distinct Sn^0 contribution arising at $\lambda > 2$ nm as shown in Fig. 5(b). This Sn^0 contribution makes up 4 % of the total peak area and confirms the assigment of Sn metal

droplets in the SEM image of Fig. 4(b) that cover a fraction of the film surface.

Hence, photoelectron spectroscopy of Y10 indicates - different from surface-sensitive Raman scattering - the presence of a few nm-thick, fully oxidized (i.e., SnO_2) layer as well as the dominant presence of SnO in the bulk, which, however, is mixed with a small fraction of metallic Sn. Please note the sensitivity of Raman spectroscopy to SnO_2 is comparably low with the excitation wavelengths used in this study. Shorter wavelengths would be required to achieve a resonant enhancement of the SnO_2 signal.

C. Summary on phase identification and refined growth window

Table I gives a summary of the identified phases in our films by the respective methods. While epitaxial, well-oriented SnO_x phases can be detected by XRD, Raman scattering is an indispensible tool to also detect polycrystalline SnO_x phases with less-well oriented crystal planes. The major SnO_x phase with $x > 1$ is Sn_3O_4 rather than SnO_2 as shown by Raman scattering. Few-nm thin surface SnO_2 was only identified by photoelectron spectroscopy and scanning electron micrographs were decisive in identifying metallic Sn (droplets). Based on the results we can delineate a growth window for phase-pure SnO at growth temperatures ranging from $400 - 300\,°C$. Whether it is possible to obtain phase-pure SnO (without additional Sn) by plasma-assisted MBE remains to be seen. The corresponding growth window would be delineated by O-fluxes between 0.12 sccm and 0.15 sccm at a growth temperature of 400°C. Hence, samples Y12 and Y15 are closest to stoichiometric, single phase SnO samples — being slightly Sn-rich and O-rich, respectively.

VI. ELECTRICAL, ELECTROTHERMAL TRANSPORT AND HOLE EFFECTIVE MASS

A. Room temperature transport properties

The charge carrier transport properties of all films were determined by room-temperature Hall measurements. Note, that the hole concentration p and drift mobility μ are generally related to the quantities extracted by Hall measurements by the – often ignored – Hall (scattering) factor r_H as: $\mu = \mu_H / r_H$ and $p = p_H \cdot r_H$.[56] The factor r_H depends on the charge carrier scattering mechanism, can range from 1 to 2 in the case of non-degenerate doping, and approaches unity for degenerate doping. In the non-degenerate case $r_H = 1.93$ for ionized impurity scattering,[56] and has been calculated to be $r_H = 1.77$ for phonon-limted transport in SnO.[57] For better comparison to literature results we are initially discussing the Hall quantities p_H and μ_H of our samples shown in Table II. All films with dominant SnO(001) identified by XRD showed p-type conductivity with varying Hall hole concentration (p_H between 1.8×10^{18} and $9.7\times10^{18}\,\mathrm{cm}^{-3}$) and resistivities ρ on the order of $1\,\Omega$cm, whereas the non-SnO films were highly resistive ($\rho > 50\,\Omega$cm). A spread of transport properties on different pieces (named ("a", "b", ...) from the same grown wafer is likely related to slight flux and/or temperature inhomogeneities, highlighting the optimization potential by finetuning growth parameters similar to what has been reported in Refs. 12,13,58.

The lower hole mobility in the films on sapphire compared to those on YSZ is likely related to the rotational domains and associated domain-boundary scattering. For the single-crystalline films on YSZ, the highest Hall mobility of $\mu_H = 6.0\,\mathrm{cm}^2/\mathrm{Vs}$ is found in Y15.

B. Temperature-dependent transport, scattering mechansim, and acceptor type

We investigated the two samples Y15 and Y12 that are closest to stoichiometric, phase-pure SnO, additionally by temperature-dependent Hall measurements between 350 and 100 K, and discuss the result in the context of available literature data. Analyzing the temperature dependence of transport properties allows us to conclude on transport mechanisms, acceptor ionization energy, and scattering mechanism. To date, the limited number of reports on temperature-dependent thin-film transistor characteristics[59–61] and temperature-dependent Hall measurements[9,10,17,58] of unintentionally-doped SnO show a variety of different transport characteristics: The observation of decreasing hole mobility with decreasing temperature has been typically associated with hopping conductivity or percolative transport,[10,59–61] whereas an increasing hole mobility has been associated with phonon-scattering limited band transport by free holes.[11,61]

Fig. 6(a) shows the extracted Hall hole mobility in Y12/b and Y15/b as function of temperature in a double-logarithmic representation. From room temperature to 100 K the mobilities of Y12/b and Y15/b increase from 2.5 and $6.0\,\mathrm{cm}^2/\mathrm{Vs}$ to 6 and $18\,\mathrm{cm}^2/\mathrm{Vs}$, respectively. The strongly increasing mobility with decreasing temperature clearly indicates dominant phonon scattering, in both samples, thus excluding hopping transport as well as a dominant influence of ionized impurity scattering (e.g. due to high compensation) or other mobility-limiting scattering mechanisms (dislocation, neutral impurity) at room temperature. In fact, the observed room-temperature mobilities of Y12/b and Y15/b are above the estimated mobility limit of $\mu_{\mathrm{H}}^{\mathrm{IIS}} \approx 2.3\,\mathrm{cm}^2/\mathrm{Vs}$ for ionized impurity scattering, taking into account $r_H = 1.93$ for IIS and the drift mobility $\mu^{\mathrm{IIS}} \approx 1.2\,\mathrm{cm}^2/\mathrm{Vs}$ predicted for an ionized impurity concentration equalling our hole concentration in Y12/b,[12] further ruling out significant ionized impurity scattering and compensation. Similar to Ref. 61 we assign optical phonon scattering to the

Table I. Summary of phase identification by the different methods. Phases in "()" denote a weak contribution.

method sample	XRD	Raman bulk	Raman surface	SEM	PES
A500	Sn_3O_4, (Sn or SnO_2)	Sn_3O_4, (SnO)	Sn_3O_4, (SnO, Sn)	porous, polycrystalline	-
A400	SnO	SnO, (Sn)	Sn_3O_4, SnO, (Sn)	crystallites (+film)	-
A300	SnO	SnO	(Sn_3O_4, SnO)	film (+ crystallites)	-
Y18	(SnO, Sn_3O_4 or Sn)	Sn_3O_4, (SnO)	Sn_3O_4	polycrystalline	-
Y15	SnO, (Sn_3O_4)	SnO, (Sn_3O_4)	Sn_3O_4	film (+ crystallites)	-
Y12	SnO	SnO	SnO, (Sn_3O_4)	film (+ Sn droplets)	-
Y10	SnO	SnO	SnO	film (+ Sn droplets)	surf. SnO_2/ bulk SnO(, Sn)

Table II. Summary of the Hall measurement results (resistivity ρ, Hall hole concentration p_H, and Hall mobility μ_H) together with the FWHM ($\triangle\omega$) of the SnO(200) reflex for all samples. Sample names in parenthesis denote non-SnO films. Hall measurements failed for A500 and Y18, likely due to a too low mobility.

sample/ piece	$\triangle\omega$ (°)	ρ (Ωcm)	p_H (10^{18}cm^{-3})	μ_H (cm^2/Vs)
(A500/a)	-	53	-	-
A400/a	1.10	1.32	4.8±1.0	1.0±0.2
A300/a	1.87	2.08	1.8 ± 0.3	1.7 ± 0.3
A300/b		1.10	2.3 ± 0.1	2.4 ± 0.1
(Y18/a)	-	217	-	-
Y15/a	0.67	0.9	2.5 ± 0.1	2.7 ± 0.1
Y15/b		0.46	2.3 ± 0.1	6.0 ± 0.2
Y12/a	0.46	0.4	4.1 ± 0.1	3.6 ± 0.1
Y12/b		0.66	3.8 ± 0.6	2.5 ± 0.4
Y10/a	0.51	0.25	9.7 ± 0.8	2.6 ± 0.2
Y10/b		0.34	3.42 ± 0.02	5.41 ± 0.03

behavior above 200 K due to the large exponent of the observed $\mu_H \propto T^{-1.31}$ and $\mu_H \propto T^{-1.75}$-dependence of Y15/b and Y12/b, respectively. In addition, first principles calculations predict phonon-scattering limited Hall hole mobilities of $\mu_H^{POP} = 106$ and $13\,cm^2/Vs$ in the c-direction and perpendicular to this direction (i.e., in the (001) plane), respectively,[57] being mainly limited by polar optical phonon scattering rather than by acoustic phonon scattering. Its anisotropy is mainly related to the anisotropy of the effective hole mass predicted by first principles calculations to be $m^*_{[001]} \approx 0.55m_e$ along the [001] direction and around $m^*_{[100]} = m^*_{[010]} \approx 3.0m_e$ in the (001)-plane with free electron mass m_e.[15,62] The phonon-limited, room-temperature hole mobilities at of Y12/b and Y15/b are ranging between reported experimental Hall hole mobilities from 2 to 3 cm^2/Vs (at Hall hole concentrations in the range of $2.5 \cdot 10^{16}$ to $2.5 \cdot 10^{17}$ cm^{-3}) on other (001)-oriented, single crystalline layers,[8,10,17] and the theoretically predicted limit in the (001)-plane. On the other hand, significantly higher room-temperature Hall mobilities have been reported for polycrystalline SnO ($\mu_H = 30$ cm^2/Vs[11] at $p_H = 7 \cdot 10^{15}$ cm^{-3}, $\mu_H =$ 19 cm^2/Vs[13] at $p_H = 2.2 \cdot 10^{17}$ cm^{-3}), which can be understood in terms of transport through crystallites with the c-axis (high-mobility direction) oriented in-plane. Interestingly, Minohara et al. reported high hole mobilities for single-crystalline (001)-oriented SnO layers (c-

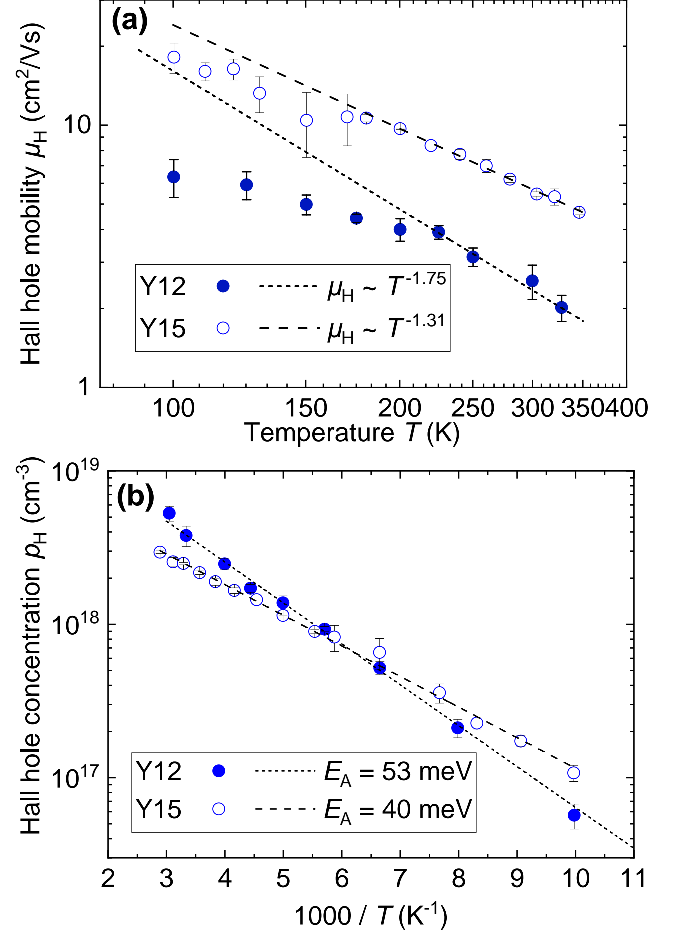

Figure 6. Hole transport properties of Y12/b and Y15/b determined by van-der-Pauw-Hall measurements at temperatures T in the range of 100 to 330 K. (a) Hall hole mobility μ_H in a double-logarithmic representation including a fitting curve of the high-temperature region. (b) Hall hole concentration p_H in an Arrhenius-type representation with associated fit and apparent activation energy E_a.

axis out-of-plane) ($\mu_{\rm H} = 15$ cm^2/Vs[58] at $p_{\rm H} = 10^{17}$ cm^{-3} and $\mu_{\rm H} = 21$ cm^2/Vs[12] at $p_{\rm H} = 7 \cdot 10^{16}$ cm^{-3}), which is difficult to explain. In addition, the decreasing Hall hole mobility with decreasing temperature reported for these layers[58] indicates that the room-temperature mobility is mainly limited by other scattering mechanisms than phonon scattering. Since phonon scattering cannot be avoided at room temperature, the high mobility may be related to a different transport mechanism, e.g. with significantly lower effective hole mass.

Fig. 6(b) shows the extracted Hall hole concentration of samples Y12/b and Y15/b as function of temperature in an Arrhenius type plot. It decreases with decreasing temperature following an activated behavior at an activation energy of $E_A = 53$ and 40 meV, respectively. In fact, most works on unintentionally-doped SnO report an activated Hall hole concentration with room-temperature values ranging from $7 \cdot 10^{15}$ to $2.5 \cdot 10^{17}$ cm^{-3} and apparent activation energies E_A in the range from 220 to 40 meV,[10,11,17] indicative of a non-degenerate doping concentration. Assuming a density-of-state (DOS) effective hole mass of $m_h^* = (m^*_{[100]} \cdot m^*_{[010]} \cdot m^*_{[001]})^{1/3} \approx 1.7 m_e$ (using the anisotropic effective mass from Ref. 15), a relative permitivity of $\epsilon_r = 18.8$,[63] and the hydrogenic Bohr radius $a_B = 0.053$ nm the Mott criterion[64] predicts a critical hole density

$$p_{\rm Mott} = [(0.26 \cdot m_h^*)/(\epsilon_r \cdot a_B \cdot m_e)]^3 \quad (1)$$

of $p_{\rm Mott} \approx 9 \cdot 10^{19}$ cm^{-3}, which indicates a non-degenerate doping concentration for all SnO layers discussed in this work and the cited literature. Notwithstanding, Minohara et al. report a temperature-independent Hall hole concentration of $p_H \approx 10^{17}$ cm^{-3} [from which we estimated $E_A \approx (-1 \pm 2)$ meV],[58] indicative of a (potentially highly compensated) degenerate acceptor concentration, suggesting distinctly different conduction mechanism from that in Y12/b, Y15/b, and most other reported literature.

For non-degenerately doped material, the assignment of the acceptor type is commonly based on the value of the activation energy E_A. Using first principles calculations Varley et al. predicted isolated tin vacancies ($V_{\rm Sn}$) and their complex with hydrogen (H-$V_{\rm Sn}$) to be potential acceptors with (0/-1) charge transition levels 155 and 70 meV above the valence band maximum, respectively, that can cause free holes in unintentionally-doped SnO.[15] These energies are considered to be identical with the acceptor ionization energy ϵ_A^0 for isolated acceptors. With increasing ionized acceptor concentration N_i, this ionization energy decreases according to $\epsilon_A = \epsilon_A^0[1-(N_i/p_{\rm Mott})^{1/3}]$[65] due to the onset of acceptor band formation, and disappears at the critical density $N_i = p_{\rm Mott}$.[66] The apparent activation energy extracted from the temperature-dependent hole concentration relates to ϵ_A by $E_A = \epsilon_A$ in the case of compensated doping or $E_A = \epsilon_A/2$ in the case of uncompensated doping.[66] Fig. 7 compares the experimentally obtained E_A from

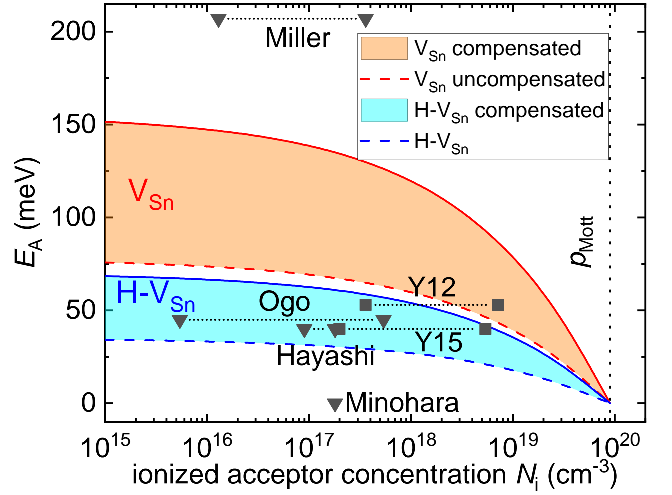

Figure 7. Comparison of the experimentally obtained apparent activation energy E_A (symbols) to theoretically prediced ones for $V_{\rm Sn}$ and H-$V_{\rm Sn}$[15] as a function of ionized acceptor concentration N_i taking into account the impact of impurity bands and compensation. Experimental data points are plotted under the assumption of no compensation ($N_i = p$) and would need to be shifted to higher N_i in case of compensation. Symbol labels indicate the source of data: "Miller",[11] "Ogo",[10] "Hayashi",[17], "Minohara",[58] "Y12" and "Y15" samples Y12/b and Y15/b of the present work.

Y12/b and Y15/b as well as Refs. 11,17,51,58 to the theoretically predicted ones for $V_{\rm Sn}$ and H-$V_{\rm Sn}$ taking into account the effect of acceptor band formation. (Note, that we calculated p from measured and reported p_H assuming a Hall factor of $r_H = 1.8$ to reflect dominant polar optical phonon scattering.) Given that the mobility behavior suggests rather uncompensated acceptors, the results for Y12/b and Y15/b match the case of $V_{\rm Sn}$ better than that of H-$V_{\rm Sn}$. The large E_A extracted from data of Ref. 11, on the other hand cannot be explained by either $V_{\rm Sn}$ or H-$V_{\rm Sn}$.[67]

C. Electrothermal transport and DOS effective hole mass

The room-temperature Seebeck coefficient S measured for all samples is shown in Tab. III. Its positive value further confirms hole conduction in all SnO samples (A300, A400, Y15, Y12, Y10), whereas A500 exhibits a negative $S-$ in agreement with the reported n-type conductivity of Sn_3O_4.[69] The high resistivity of Y18 did not allow for a reliable Seebeck measurement.

The Seebeck coefficient is related to the bulk carrier concentration and can be used as an alternative to Hall measurements for the estimation of p if the transport mechanism is known. For example, in oxides with hole transport by small-polaron hopping S can be related to p by:

Table III. Calculated DOS effective hole mass (m_h^*) based on p_H and S from Hall and Seebeck measurements for all SnO samples as data from literature using Eq. 3 and the related formalism described in Ref. 25. A Hall factor of $r_H = 1.8$ is assumed. The limiting cases polar optical phonon scattering (POPS, $r = 0.5$) and ionized impurity scattering (IIS, $r = 1.5$) are considered. For comparison, the hole concentration p_{SPH} calculated from S using Eq. 2 is given to test the hypothesis of transport by small polaron hopping.

sample/ piece	p_H ($\mathbf{10^{18}/cm^3}$)	p ($\mathbf{10^{18}/cm^3}$)	**S** (µV/K)	p_{SPH} ($\mathbf{10^{18}/cm^3}$)	$\boldsymbol{m_h^*}$ ($\boldsymbol{m_e}$) POPS, $r = 0.5$	$\boldsymbol{m_h^*}$($\boldsymbol{m_e}$) IIS, $r = 1.5$
(A500/a)	-	-	-266±7	-	-	-
A400/a	4.8 ± 1.0	8.6 ± 1.80	616±26	42 ± 14	7.94	4.10
A300/a	1.8 ± 0.3	3.24 ± 0.54	597±17	52 ± 11	3.58	1.85
(Y18/a)	-	-	-	-	-	-
Y15/a	2.5 ± 0.1	4.50 ± 0.18	480±45	228 ± 109	1.82	0.96
Y12/b	3.8 ± 0.6	6.8 ± 1.1	523±7	122 ± 10	3.33	1.74
Y10/a	9.7 ± 0.8	17.46 ± 1.44	543±9	97 ± 10	7.27	3.78
Hayashi[17]	0.1	0.18	763	7.56	1.88	0.96
Hosono[68]	0.71	1.28	479	202.9	0.78	0.41
Miller[11]	0.013	0.023	630	35.3	0.17	0.09
Becker[9]	0.0046	0.0083	550	89.3	0.05	0.02
Ogo[51]	0.25	0.45	1990	2×10^{-6}	45766	23497

$$S_{SPH} = \frac{k_B}{e} \ln[(2 - 2c)/c] \tag{2}$$

with Boltzmanns constant k_B, electronic charge e, and the fraction of occupied carrier sites $c = p/N$, i.e., the ratio of hole concentration p to concentration N of sites that can be occupied by a hole (e.g., the Sn-site in SnO).[3] For example, this relation has been used to estimate p from the measured S in doped p-type oxides whose hole mobility is too low ($\mu \ll 1\,\text{cm}^2/\text{Vs}$) to allow for Hall measurements, i.e., in Cr_2O_3:Mg,[3] $LaCrO_3$:Sr,[4] and NiO:Li.[1] For the band-like transport a different relation $S = S(p, m_h^*, r)$ holds which has an additional dependence on the DOS effective hole mass (m_h^*) and the Seebeck scattering parameter (r). For non-degenerate doping (which applies to our films, since $p \ll p_{\text{Mott}}$) it reads as:[70]

$$S_{nd} = \frac{k_B}{e} \cdot \left(r + \frac{5}{2} - \frac{E_{VBM} - E_F}{k_B T} \right) \tag{3}$$

with the term ($E_{VBM} - E_F$) denoting the distance between Fermi level E_F and valence band maximum E_{VBM} being related to the hole concentration p through semiconductor statistics (as described in detail in Ref. 25) using the valence band DOS parametrized by m_h^*. The Seebeck scattering parameter varies between $r = -0.5$ for dominant acoustic phonon scattering and $r = 1.5$ for dominant ionized impurity scattering. Optical phonon scattering is typically described by a scattering parameter of $r = 0.5$.[71]

Since no experimental values of m_h^* of SnO have been published to date we are using the combination of p_H determined by Hall measurements and measured Seebeck coefficient S to estimate m_h^* based on Eq. 3 for the different r as previously demonstrated for the n-type semiconducting oxide In_2O_3.[25] The results are shown in Tab. III along with the hypothetical hole concentration p_{SPH} derived from S under the assumption of small polaron hopping using Eq. 2 and $N = 2.66 \cdot 10^{22}\,\text{cm}^{-3}$, the concentration of Sn-atoms. For comparison we have added p_H and associated S reported in the literature.[9,11,17,51,68] The drastic discrepancy of the extracted p_{SPH} assuming small polaron hopping and measured p_H demonstrates for all samples, that the transport is not well described by small polaron hopping. This corroborates the assumption of band transport by free holes and consequently, the applicability of the used model according to Eq. 3. Assuming hole transport to be mainly limited by polar optical phonon scattering ($r = 0.5$) or ionized impurity scattering ($r = 1.5$) we extracted values of the DOS effective hole mass m_h^* between $\approx 1\,m_e$ and $\approx 8\,m_e$ for SnO our films and that of Ref. 17. These values are in fair agreement with the theoretically predicted $m_h^* = 1.7\,m_e$, and can be seen as an experimental confirmation of its order of magnitude. Published p_H and S from Refs. 9,11,68, would result in significantly lower values of m_h^*. This discrepancy may be related to different transport mechanism or an inhomogeneous carrier distribution, for example due to the confinement in a thin accumulation layer. The actual hole concentration in the accumulation layers would be higher than that extracted from Hall measurements (that assume the carriers to be spread across the entire film thickness),[72] and would consequently lead to a larger extracted DOS effective hole mass.

VII. STABILITY OF THE SNO PHASE AFTER GROWTH

The thermal stability of SnO films is highly relevant for their application with respect to the temperature bud-

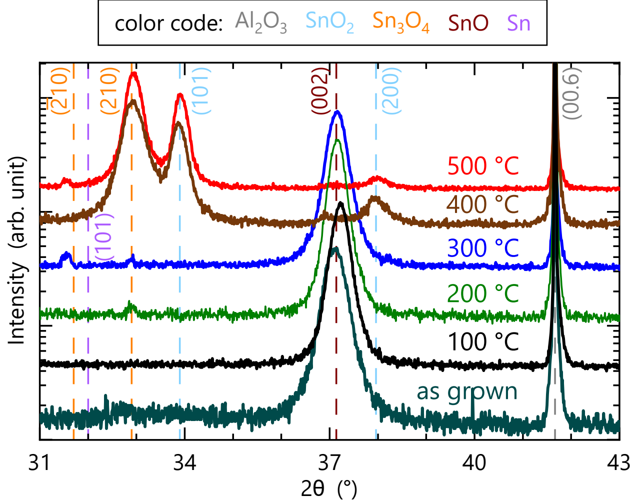

Figure 8. Symmetric XRD $2\theta - \omega$ scans of pieces of A400 annealed in nitrogen at temperatures ranging from 100 °C to 500 °C. For reference purposes the scan of the as grown A400 is shown.

Table IV. Results of Hall measurements on pieces of A400 and A400* annealed in nitrogen (N_2), oxygen (O_2) and forming gas (FG) at different temperatures. Annealing temperature $T_{ann.}$ ("a.g." denotes as-grown, the "*" denotes pieces of sample A400*), resistivity ρ, Hall hole concentration p_H. (negative values denote n-type conductivity), and Hall hole mobility μ_H.

$T_{ann.}$ (°C)	gas	ρ (Ωcm)	p_H (10^{18}cm^{-3})	μ_H (cm^2/Vs)
a.g.	-	1.0	3.9 ± 0.6	1.7 ± 0.3
a.g.*	-	1.9	2.7 ± 0.3	1.2 ± 0.3
100	N_2	0.8	6.5 ± 0.8	1.2 ± 0.2
200	N_2	0.6	6.8 ± 1.3	1.5 ± 0.3
300*	N_2	1.2	3.5 ± 0.2	1.5 ± 0.1
300*	O_2	1.3	3.6 ± 0.5	1.3 ± 0.2
300*	FG	1.1	2.5 ± 0.1	2.2 ± 0.1
400	N_2	0.1	- 40 ± 4	1.0 ± 0.1
400*	O_2	0.2	-1.9 ± 0.2	7.3 ± 0.7
400*	FG	0.5	-5.8 ± 0.6	5.5 ± 0.5
500	N_2	0.1	-5.8 ± 0.6	8.6 ± 0.9

get during device processing, e.g., contact annealing, and the operation temperature, e.g., in power devices. An early work by Moh reports SnO to be stable with respect to disproportionation or oxidation only up to 270°C.[73] In contrast, a number of later publications describe the transformation of polycrystalline SnO into SnO_2 upon annealing in different atmospheres to proceed at temperatures between 400 °C and 550 °C.[40,74–78]: Geurts et al. describe the oxidation process from SnO to SnO_2 through the intermediate stoichiometries e.g., Sn_3O_4 or Sn_2O_3 at temperatures ranging from 450 to 650°C to start by an internernal displacement of oxygen (disproportionation) followed by oxidation through incorporation of external oxygen.[40]. For the complete oxidation to SnO_2 Reddy et al. reported a temperature of 600 °C during a two hour annealing in oxygen.[76] On the other hand, Pei et al. reported highly stable SnO layers reaching their highest crystalline quality during RTA (with unspecified annealing time) at 700 °C in nitrogen.[16] Interestingly, Yabuta et al. demonstrated that a SiO_x capping layer preseves the SnO layer by preventing oxygen exchange with the environment using annealing experiments in nitrogen, oxygen and air at 400 °C.[77] We note, however, that a capping layer cannot prevent disproportionation of the film at temperatures above ≈ 400 °C (cf. Fig1).

We investigated the thermal stability our SnO films with the example of samples A400 and A400*. Sample A400* is an additional sample grown under the same growth conditions as A400, showing the same XRD reflexes and exhibiting similar transport properties. Different pieces of these samples were annealed by RTA at temperatures between 100 °C and 500 °C for 10 minutes in nitrogen, oxygen and forming gas ($N_2 + H_2$) atmospheres. In Fig. 8 symmetric out-of-plane XRD $2\theta - \omega$ scans of A400 annealed in nitrogen at various temperatures shows preservation of the SnO layer up to 300°C and its transformation into mainly Sn_3O_4[79] and SnO_2 for temperatures of 400 °C and above, in good agreement with the phase diagram in Fig. 1. The effect of annealing treatments in different atmospheres on the transport properties is shown in Tab. IV. Irrespective of the atmosphere, P-type conductivity is preserved for annealing at 300°C and below with only small quantitative changes that may also be related to inhomogeneity across the wafer. More significantly, n-type conductivity is observed after annealing at 400 °C and above for all tested atmospheres, in agreement with the phase change seen by the XRD results of the samples annealed in N_2.

In addition, the stability over time was investigated by long-term Hall measurements of Y12/a under storage in ambient air. The measured Hall hole concentration, mobility and sheet resistance are summarized in Fig. 9 for a period of 120 days. Only a slight change of the electrical properties is found and a stabilization is indicated after about 40 days. No change to n-type transport was observed. The long-term stability of the p-type transport in our SnO films was confirmed in A400/a, A400*, and Y15/a that were re-measured after a period of 14, 11, and 15 months, respectively.

These results identify an upper limit for the processing or operating temperature between 300 and 400 °C for devices using SnO layers. Slight changes of the hole density with time or annealing need further detailed investigation as they may relate to the unintentional doping. The independency from the annealing atmosphere (with and without O_2) suggests the change to n-type transport upon annealing at 400 °C and above to occur by disproportionation rather than oxidation. Thus, a capping layer would not allow processing temperatures of 400 °C and

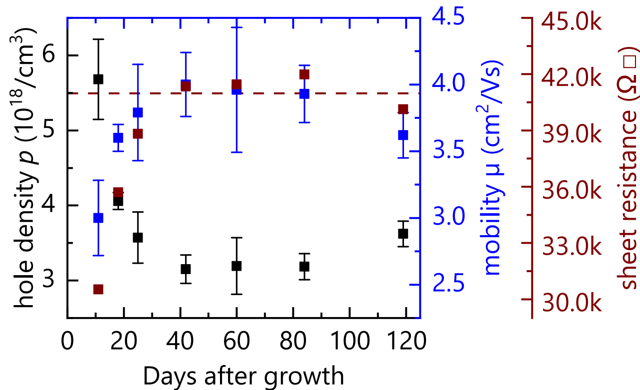

Figure 9. Hall hole concentration (black squares), sheet resistance (brown squares) and Hall hole mobility (blue squares) of Y12 stored in ambient atmosphere for up to 120 days after the growth run. The dashed brown line indicates the saturation of the sheet resistance after 20 to 40 days.

above. Long-term device operation using SnO layers is feasable at room temperature in ambient air. According to the equilibrium phase diagram (Fig. 1) device operation should be feasable even up to 400 °C, which still needs to be validated experimentally by long-term aging studies of actual films at such temperatures.

VIII. CONCLUDING DISCUSSION

Two key features of SnO are its metastability with respect to the formation of (secondary) SnO_x phases with $x = 0$ or $1 < x \leq 2$ as well as its anisotropic, comparably high hole mobility.

A. Metastability

The growth of the metastable p-type semiconducting oxide SnO is challenged by its metastability, which we described by a theoretically established[27] phase diagram showing regions containing Sn, SnO, and SnO_2. Adressing this metastability we presented a rapid, experimental in-situ approach[22] to delineate the SnO growth window in plasma-assisted molecular beam epitaxy based on the understanding that SnO_2 grows through the intermediate formation of its suboxide SnO.[28] A critical assessment of potentially present secondary phases was found to require the combination of different experimental methods: While XRD is only sensitive to epitaxially well-oriented phases (mainly SnO in our case), Raman spectroscopy is essential, in particular for the identification of Sn_3O_4,[34] and SEM is key for the detection of Sn (droplets). Different from the phase diagram, our experimental results point towards the formation of Sn_3O_4 rather than SnO_2 as secondary phase for slightly O-rich growth conditions. Near surface Sn_3O_4 detected by surface-sensitive Raman spectroscopy and a few-nm thick surface SnO_2 layer detected by XPS are likely related to the post-growth cooldown in oxygen plasma, and may possibly be avoided by cooldown in vacuum. Layers with the closest stoichiometry to SnO contain a fraction of either Sn_3O_4 or Sn as secondary phase, necessitating a control of the Sn-to-O-plasma flux ratios better than 10 % used in this study to achieve complete phase purity. Room temperature hole transport properties and Seebeck coefficient of these slightly O-rich and Sn-rich layers (samples Y12 and Y15) are very similar, suggesting a minor impact of the secondary phases. A significant enhancement of the hole mobility due to a secondary Sn-phase reported in Ref. 13 was not reproduced by our Sn-rich films (Y12 and Y10). Annealing experiments in different atmospheres confirm structural and electrical stability of SnO layers up to temperatures between 300 and 400 °C (in fair agreement with the phase diagram), defining an upper limit for the thermal budget of processing SnO-containing devices.

B. Hole mobility

At present the understanding of the hole mobility in SnO is rather limited: The highest room temperature hole mobility in our (001)-oriented films of 6.0 cm^2/Vs at a hole concentration of $2.3 \cdot 10^{18}$ cm^{-3} in Y15/b was found to be mainly limited by phonon scattering in non-degenerate band transport. The same holds true for the lower mobility of 2.5 cm^2/Vs in Y12/b at similar hole concentration. This behavior is, however, inconsistent with the significantly higher theoretically predicted Hall mobility limit due to phonons of $\mu_H^{POP} \approx 13$ cm^2/Vs for this orientation,[57] as well as the significantly lower predicted Hall mobility for ionized impurity scattering of $\mu_H^{IIS} \approx 2.3$ cm^2/Vs for an ionized acceptor concentration matching our hole concentration.[12] Moreover, for the same orientation reports by Minohara et al.[12,58] of $\mu_H \approx$ 10 to 21 cm^2/Vs at lower hole concentration in single-crystalline layers document a degenerate behavior,[58] and hole transport limited by other mechanisms than phonon scattering.[12,58] The contradiction of these results to our phonon-limited transport at an even higher hole concentration suggests different types of transport, possibly related to a significantly lower effective hole mass either through a modified band structure or a defect band in the samples by Minohara et al. An initial theoretical explanation involving the effect of Sn interstitials and O vacancies on band structure has been given by Granato et al..[80] Other reported high hole mobilities of $\mu_H \approx$ 19 and 30 cm^2/Vs in the literature for polycrystalline material[11,13] may be related to transport through crystallites with the high-mobility [001]-direction oriented in-plane, for which the theoretically predicted Hall mobility limit due to phonons is $\mu_H^{POP} \approx 106$ cm^2/Vs.[57] While the anisotropy of the effective-mass and transport have been experimentally determined and shown to match for the rutile n-type oxide SnO_2,[81–83] similar experimental stud-

ies are missing for SnO to date.

ACKNOWLEDGMENTS

We would like to thank H.-P. Schönherr and C. Stemmler for MBE support, A.-K. Bluhm for SEM imaging, S. Rauwerdink and A. Riedel for sample processing, and M. Heilmann for critically reading the manuscript. This work was performed in the framework of GraFOx, a Leibniz-ScienceCampus partially funded by the Leibniz association. M.B. and J.F. gratefully acknowledge financial support by the Leibniz association. We are grateful to HiSOR, Hiroshima University, and JAEA/SPring-8 for the development of HAXPES at BL15XU of SPring-8. The HAXPES measurements were performed under the approval of the NIMS Synchrotron X-ray Station (Proposal No. 2018B4600, and 2019A4601).

REFERENCES

[1]J.-Y. Zhang, W. Li, R. L. Z. Hoye, J. MacManus-Driscoll, M. Budde, O. Bierwagen, L. Wang, Y. Du, M. Wahila, L. F. Piper, T.-L. Lee, H. Edwards, V. R. Dhanak, and H. Zhang, J. Mater. Chem. C **6**, 2275 (2018).
[2]R. Karsthof, M. Grundmann, A. M. Anton, and F. Kremer, Physical Review B **99**, 2 (2019).
[3]L. Farrell, K. Fleischer, D. Caffrey, D. Mullarkey, E. Norton, and I. V. Shvets, Phys. Rev. B **91**, 125202 (2015).
[4]K. H. L. Zhang, Y. Du, A. Papadogianni, O. Bierwagen, S. Sallis, L. F. J. Piper, M. E. Bowden, V. Shutthanandan, P. V. Sushko, and S. A. Chambers, Advanced Materials **27**, 5191 (2015).
[5]K. H. L. Zhang, K. Xi, M. G. Blamire, and R. G. Egdell, J. Phys. Condens. Matter **28**, 1 (2016).
[6]H. Kawazoe, M. Yasukawa, H. Hyodo, M. Kurita, H. Yanagi, and H. Hosono, Nature **389**, 939 (1997).
[7]Z. Wang, P. K. Nayak, J. A. Caraveo-Frescas, and H. N. Alshareef, Advanced Materials **28**, 3831 (2016).
[8]A. B. Mei, L. Miao, M. J. Wahila, G. Khalsa, Z. Wang, M. Barone, N. J. Schreiber, L. E. Noskin, H. Paik, T. E. Tiwald, Q. Zheng, R. T. Haasch, D. G. Sangiovanni, L. F. J. Piper, and D. G. Schlom, Phys. Rev. Mater. **3**, 105202 (2019).
[9]M. Becker, R. Hamann, D. Hartung, C. Voget-Grote, S. Graubner, P. Hoffmann, C. Ronning, A. Polity, and P. J. Klar, Journal of Applied Physics **125**, 085703 (2019).
[10]Y. Ogo, H. Hiramatsu, K. Nomura, H. Yanagi, T. Kamiya, M. Hirano, and H. Hosono, Appl. Phys. Lett. **93**, 032113 (2008).
[11]S. A. Miller, P. Gorai, U. Aydemir, T. O. Mason, V. Stevanović, E. S. Toberer, and G. J. Snyder, Journal of Materials Chemistry C **5**, 8854 (2017).
[12]M. Minohara, A. Samizo, N. Kikuchi, K. K. Bando, Y. Yoshida, and Y. Aiura, The Journal of Physical Chemistry C **124**, 1755 (2019).
[13]J. A. Caraveo-Frescas, P. K. Nayak, H. A. Al-Jawhari, D. B. Granato, U. Schwingenschlögl, and H. N. Alshareef, ACS Nano **7**, 5160 (2013).
[14]A. Togo, F. Oba, I. Tanaka, and K. Tatsumi, Phys. Rev. B **74**, 195128 (2006).
[15]J. B. Varley, A. Schleife, A. Janotti, and C. G. Van de Walle, Applied Physics Letters **103**, 082118 (2013).
[16]Y. Pei, W. Liu, J. Shi, Z. Chen, and G. Wang, J. Electron. Mater. **45**, 5967 (2016).
[17]H. Hayashi, S. Katayama, R. Huang, K. Kurushima, and I. Tanaka, Phys. Status Solidi Rapid Res. Lett. **9**, 192 (2015).
[18]M. Li, L. Zheng, M. Zhang, Y. Lin, L. Li, Y. Lu, G. Chang, P. J. Klar, and Y. He, Applied Surface Science **466**, 765 (2019).
[19]S. Hishita, P. Janecek, and H. Haneda, Journal of Crystal Growth **312**, 3046 (2010).
[20]A. Nikiforov, V. Timofeev, V. Mashanov, I. Azarov, I. Loshkarev, V. Volodin, D. Gulyaev, I. Chetyrin, and I. Korolkov, Applied Surface Science **512**, 145735 (2020).
[21]G. Hoffmann, M. Budde, P. Mazzolini, and O. Bierwagen, APL Materials **8**, 031110 (2020).
[22]P. Vogt and O. Bierwagen, Applied Physics Letters **106**, 081910 (2015).
[23]S. Ueda, Y. Katsuya, M. Tanaka, H. Yoshikawa, Y. Yamashita, S. Ishimaru, Y. Matsushita, K. Kobayashi, R. Garrett, I. Gentle, K. Nugent, and S. Wilkins, in *AIP Conf. Proc.*, Vol. 1234 (AIP, 2010) p. 403.
[24]T. Nagata, O. Bierwagen, Z. Galazka, S. Ueda, M. Imura, Y. Yamashita, and T. Chikyow, Japanese Journal of Applied Physics **58**, 080903 (2019).
[25]N. Preissler, O. Bierwagen, A. T. Ramu, and J. S. Speck, Phys. Rev. B **88**, 085305 (2013).
[26]C. Golz, Z. Galazka, J. Lähnemann, V. Hortelano, F. Hatami, W. T. Masselink, and O. Bierwagen, Physical Review Materials **3**, 124604 (2019).
[27]C. Bale, E. Bélisle, P. Chartrand, S. Decterov, G. Eriksson, A. Gheribi, K. Hack, I.-H. Jung, Y.-B. Kang, J. Melançon, A. Pelton, S. Petersen, C. Robelin, J. Sangster, P. Spencer, and M.-A. V. Ende, Calphad **54**, 35 (2016).
[28]P. Vogt and O. Bierwagen, Phys. Rev. Materials **2**, 120401 (2018).
[29]M. Y. Tsai, M. E. White, and J. S. Speck, Journal of Applied Physics **106**, 024911 (2009).
[30]V. T. Deshpande and D. B. Sirdeshmukh, Acta Crystallographica **14**, 355 (1961).
[31]W. H. Baur, Acta Crystallographica **9**, 515 (1956).
[32]J. Pannetier and G. Denes, Acta Crystallographica Section B Structural Crystallography and Crystal Chemistry **36**, 2763 (1980).
[33]A. Seko, A. Togo, F. Oba, and I. Tanaka, Physical Review Letters **100** (2008), 10.1103/physrevlett.100.045702.
[34]B. Eifert, M. Becker, C. T. Reindl, M. Giar, L. Zheng, A. Polity, Y. He, C. Heiliger, and P. J. Klar, Phys. Rev. Materials **1**, 014602 (2017).
[35]F. Lawson, Nature **215**, 955 (1967).
[36]T. A. White, M. S. Moreno, and P. A. Midgley, Zeitschrift für Kristallographie **225** (2010), 10.1524/zkri.2010.1210.
[37]G. Murken and M. Trömel, Zeitschrift für anorganische und allgemeine Chemie **397**, 117 (1973).
[38]X. Kuang, T. Liu, W. Zeng, X. Peng, and Z. Wang, Materials Letters **165**, 235 (2016).
[39]O. M. Berengue, R. A. Simon, A. J. Chiquito, C. J. Dalmaschio, E. R. Leite, H. A. Guerreiro, and F. E. G. Guimarães, Journal of Applied Physics **107**, 033717 (2010).
[40]J. Geurts, S. Rau, W. Richter, and F. Schmitte, Thin Solid Films **121**, 217 (1984).
[41]H. Song, S.-Y. Son, S. K. Kim, and G. Y. Jung, Nano Research **8**, 3553 (2015).
[42]R. S. Katiyar, P. Dawson, M. M. Hargreave, and G. R. Wilkinson, Journal of Physics C: Solid State Physics **4**, 2421 (1971).
[43]T. Lan, C. W. Li, and B. Fultz, Phys. Rev. B **86**, 134302 (2012).
[44]S. D. Balgude, Y. A. Sethi, B. B. Kale, N. R. Munirathnam, D. P. Amalnerkar, and P. V. Adhyapak, RSC Advances **6**, 95663 (2016).
[45]H. Olijnyk, Physical Review B **46**, 6589 (1992).
[46]M. Cardona, *Light Scattering in Solids II*, edited by M. Cardona and G. Güntherodt (Springer Berlin Heidelberg, 1982) p. 9.
[47]A. Compaan and H. J. Trodahl, Physical Review B **29**, 793 (1984).
[48]M. Feneberg, C. Lidig, K. Lange, R. Goldhahn, M. D. Neumann, N. Esser, O. Bierwagen, M. E. White, M. Y. Tsai, and J. S. Speck, Applied Physics Letters **104**, 231106 (2014).

[49]M. Grundmann, T. Böntgen, and M. Lorenz, Phys. Rev. Lett. **105**, 146102 (2010).
[50]M. Manikandan, T. Tanabe, P. Li, S. Ueda, G. V. Ramesh, R. Kodiyath, J. Wang, T. Hara, A. Dakshanamoorthy, S. Ishihara, K. Ariga, J. Ye, N. Umezawa, and H. Abe, ACS Applied Materials & Interfaces **6**, 3790 (2014).
[51]Y. Ogo, H. Hiramatsu, K. Nomura, H. Yanagi, T. Kamiya, M. Kimura, M. Hirano, and H. Hosono, Phys. Status Solidi A **206**, 2187 (2009).
[52]L. Kövér, G. Moretti, Z. Kovács, R. Sanjinés, I. Cserny, G. Margaritondo, J. Pálinkás, and H. Adachi, Journal of Vacuum Science & Technology A: Vacuum, Surfaces, and Films **13**, 1382 (1995).
[53]J. F. Moulder, W. F. Stickle, P. E. Sobol, and K. D. Bomben, *Handbook of X Ray Photoelectron Spectroscopy*, edited by J. Chastain and R. C. K. Jr. (Physical Electronics, Inc., 1995).
[54]W. Xia, H. Wang, X. Zeng, J. Han, J. Zhu, M. Zhou, and S. Wu, CrystEngComm **16**, 6841 (2014).
[55]A. Y. Mohamed, S. J. Lee, Y. Jang, J. S. Kim, C. S. Hwang, and D.-Y. Cho, Journal of Physics: Condensed Matter **32**, 065502 (2019).
[56]S. M. Sze and K. K. Ng, *Physics of Semiconductor Devices* (Wiley Inderscience, 2007).
[57]Y. Hu, J. Hwang, Y. Lee, P. Conlin, D. G. Schlom, S. Datta, and K. Cho, Journal of Applied Physics **126**, 185701 (2019).
[58]M. Minohara, N. Kikuchi, Y. Yoshida, H. Kumigashira, and Y. Aiura, Journal of Materials Chemistry C **7**, 6332 (2019).
[59]E. Fortunato, R. Barros, P. Barquinha, V. Figueiredo, S.-H. K. Park, C.-S. Hwang, and R. Martins, Appl. Phys. Lett. **97**, 052105 (2010).
[60]J. Zhang, X. Kong, J. Yanga, Y. Li, J. Wilson, J. Liu, Q. Xin, Q. Wang, and A. Song, Appl. Phys. Lett. **108**, 263503 (2016).
[61]H.-J. Kim, C.-Y. Jeong, S.-D. Bae, J.-H. Lee, and H.-I. Kwon, IEEE Electron Device Lett. **38**, 473 (2017).
[62]V.-A. Ha, F. Ricci, G.-M. Rignanese, and G. Hautier, Journal of Materials Chemistry C **5**, 5772 (2017).
[63]X. Li, L. Liang, H. Cao, R. Qin, H. Zhang, J. Gao, and F. Zhuge, Applied Physics Letters **106**, 132102 (2015).
[64]N. Mott, Proceedings of the Royal Society of London. A. Mathematical and Physical Sciences **382**, 1 (1982).
[65]G. L. Pearson and J. Bardeen, Physical Review **75**, 865 (1949).
[66]M. Grundmann, *The Physics of Semiconductors* (Springer, 2006).
[67]We note that the activation energy of $\approx 0.09\,\mathrm{eV}$ stated in reference 11 does not match the data presented in that paper. We believe that it was likely erroneously extracted from an Arrhenius-plot using $\log p$ instead of $\ln p$.
[68]H. Hosono, Y. Ogo, H. Yanagi, and T. Kamiya, Electrochemical and Solid-State Letters **14**, H13 (2011), http://esl.ecsdl.org/content/14/1/H13.full.pdf+html.
[69]P. H. Suman, E. Longo, J. A. Varela, and M. O. Orlandi, Journal of Nanoscience and Nanotechnology **14**, 6662 (2014).
[70]K. Seeger, *Semiconductor Physics*, 9th ed. (Springer, 2004).
[71]D. S. Ginley, ed., *Handbook of Transparent Conductors* (Springer US, 2011).
[72]A. Papadogianni, M. E. White, J. S. Speck, Z. Galazka, and O. Bierwagen, Applied Physics Letters **107**, 252105 (2015).
[73]G. H. Moh, Chem d. Erde **33**, 243 (1974).
[74]T. Oyabu, Journal of Applied Physics **53**, 2785 (1982).
[75]D. Das and R. Banerjee, Thin Solid Films **147**, 321 (1987).
[76]M. H. M. Reddy, S. R. Jawalekar, and A. N. Chandorkar, Thin Solid Films **169**, 117 (1989).
[77]H. Yabuta, N. Kaji, R. Hayashi, H. Kumomi, K. Nomura, T. Kamiya, M. Hirano, and H. Hosono, Applied Physics Letters **97**, 072111 (2010).
[78]S.-S. Lin, S.-Y. Fan, and Y.-S. Tsai, Ceramics International **43**, 1802 (2017).
[79]S. Balgude, Y. Sethi, B. Kale, D. Amalnerkar, and P. Adhyapak, Materials Chemistry and Physics **221**, 493 (2019).
[80]D. B. Granato, J. A. Caraveo-Frescas, H. N. Alshareef, and U. Schwingenschlögl, Applied Physics Letters **102**, 212105 (2013).
[81]K. J. Button, C. G. Fonstad, and W. Dreybrodt, Phys. Rev. B **4**, 4539 (1971).
[82]M. Feneberg, C. Lidig, K. Lange, M. E. White, M. Y. Tsai, J. S. Speck, O. Bierwagen, and R. Goldhahn, physica status solidi (a) **211**, 82 (2014).
[83]O. Bierwagen and Z. Galazka, Applied Physics Letters **112**, 092105 (2018).